Quantum Transport in Graphene Nanoribbons: Effects of Edge Reconstruction and Chemical Reactivity

Simon M.-M. Dubois,[†,*] Alejandro Lopez-Bezanilla,[‡] Alessandro Cresti,[§,⊥] François Triozon,[§] Blanca Biel,[¶] Jean-Christophe Charlier,[†] and Stephan Roche[⊥,#,▽]

[†]Institute of Condensed Matter and Nanosciences (IMCN), European Theoretical Spectroscopy Facility (ETSF), Université Catholique de Louvain, Place Croix du Sud 1 (PCPM-Boltzmann), 1348 Louvain-la-Neuve, Belgium, [‡]CEA, INAC, SPSMS, 17 rue des Martyrs, 38054 Grenoble Cedex 9, France, [§]CEA, LETI, MINATEC, F38054 Grenoble, France, [⊥]CEA, INAC, SP2M, L_sim, 17 rue des Martyrs, 38054 Grenoble Cedex 9, France, [¶]Departamento Electrónica y Tecnología de Computadores, Facultad de Ciencias, & CITIC, Universidad de Granada, E-18071 Granada, Spain, [#]Institute for Materials Science, TU Dresden, D-01062 Dresden, Germany, and [▽]CIN2 (CSIC-ICN), Campus de la U.A.B., 08193 Bellaterra, Barcelona, Spain

ABSTRACT We present first-principles transport calculations of graphene nanoribbons with chemically reconstructed edge profiles. Depending on the geometry of the defect and the degree of hydrogenation, spectacularly different transport mechanisms are obtained. In the case of monohydrogenated pentagon (heptagon) defects, an effective acceptor (donor) character results in strong electron−hole conductance asymmetry. In contrast, weak backscattering is obtained for defects that preserve the benzenoid structure of graphene. Based on a tight-binding model derived from *ab initio* calculations, evidence for large conductance scaling fluctuations are found in disordered ribbons with lengths up to the micrometer scale.

KEYWORDS: graphene nanoribbons · quantum transport · edge reactivity · density-of-state

The exploration of the electronic properties of carbon-based materials has witnessed a relentless pace since the discovery of carbon nanotubes[1,2] and two-dimensional graphene materials.[3,4] Graphene nanoribbons (GNRs) are strips of graphene with widths varying from a few to several hundreds of nanometers,[5−8] presenting particular interest for the development of carbon-based nanoelectronics.[9−13] In contrast to carbon nanotubes, GNRs exhibit a high degree of edge chemical reactivity, which, for instance, prevents the existence of truly metallic nanoribbons.[14−17] Additionally, the discrepancy between the theoretical electronic confinement gap and the experimentally measured transport gap[9] has been attributed to localized states induced by edge disorder.[18−21]

To date, most transport studies of edge disordered GNRs have assumed simplified defect topologies.[18−21] However, recent *ab initio* calculations have unveiled a much larger complexity of edge reconstructions and edge chemistry.[22−25] Several experimental studies have also reported on the characterization of individual edge defects by means of either Raman, scanning tunneling and transmission electron microscopies.[26−28] Finally, the control of monatomic hydrogen deposition on a graphene surface has revealed the possibility to tune a metal−insulator transition.[29,30] Accordingly, it is of great importance to investigate the impact of realistic edge defect topologies and the role of hydrogenation on charge transport properties of long and disordered GNRs.

In this paper, we investigate the electronic transport in realistic edge disordered armchair GNRs (aGNRs). Using density functional theory combined with coherent quantum transport models, the transport properties of aGNRs are predicted to strongly depend on the geometry of the reconstructed edge profile and local defect chemical reactivity. The effect of single edge defects ranges from a full suppression of either hole or electron conduction to a vanishing contribution of backscattering. Besides, hydrogenation of the chemically active defects is found to globally restore electron and hole conduction. Finally, owing to the derivation of a suited tight-binding model, mesoscopic transport calculations of disordered ribbons with lengths up to several micrometers are achieved, and conduction is found to change from metallic to insulating regime depending on the geometry and density of edge defects.

RESULTS AND DISCUSSION

Following the nomenclature of Son *et al.*,[14] we refer to an aGNR made up by

*Address correspondence to smmfnd2@cam.ac.uk.

Received for review January 6, 2010 and accepted March 19, 2010.

Published online March 31, 2010. 10.1021/nn100028q

© 2010 American Chemical Society

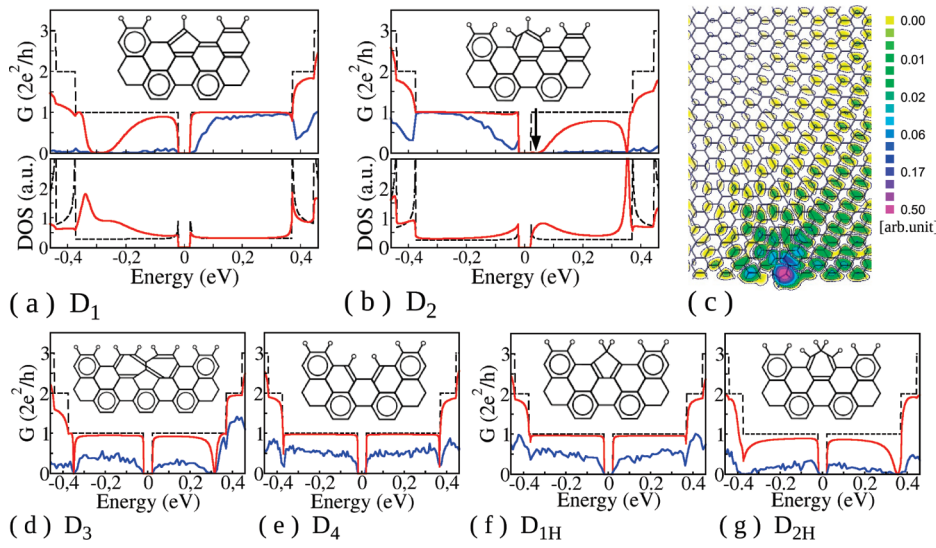

Figure 1. Conductance profiles of 35-aGNR for six different edge geometries: pristine ribbon (dashed black lines), single defect (red lines), and average conductance for 500 nm long aGNRs containing 30 defects (blue lines). The total density-of-states (DOS) computed in the presence of single pentagon and heptagon defects are also shown. (Top panel) Edge defect topologies containing odd-membered rings: (a) a single pentagon defect-D_1, (b) a single heptagon-D_2. (c) Spatial representation of the transmission eigenchannel at the energy marked by an arrow in panel b. (Bottom panel) Edge reconstruction involving only benzenoid defects: (d) 2 heptagons and 1 pentagon, D_3, (e) small hole due to a dimer extraction, D_4. (f) D_{1H} and (g) D_{2H} denote the dihydrogenated pentagon and heptagon, respectively. Insets: Clar's sextet representation for each edge geometry.

N dimer lines as an *N*-aGNR. We have focused on the 35-aGNR, with a width of 4.2 nm, but our conclusions remain valid for wider aGNRs. The edge patterns considered in this study are displayed in Figure 1 using Clar's sextet representation. Among all the different studied defects, the reconstructed geometries that preserve the benzenoid structure of pristine aGNRs turn out to weakly impact the transmission. The most striking example is the conductance profile of the D_4 defect (see Figure 1e). The conductance remains very close to its maximum quantized value as found in the pristine case, with weak backscattering mainly observed in higher subbands. Slightly differently, the double heptagon and pentagon defect (D_3) exhibits two conductance suppression dips (Figure 1d), symmetric with respect to the charge neutrality point, thus recalling the signature of a sp^3-type defect.[31] Other topologies preserving the benzenoid structure also yield very similar results to those of the D_3 and D_4 defects (not shown here). In large contrast, edge defects containing monohydrogenated odd-membered rings convey much stronger backscattering efficiency. Conductance fingerprints for single reconstructed pentagon and heptagon defects are shown in Figure 1a and Figure 1b, respectively. Interestingly, a marked acceptor (donor) character develops for the pentagon (heptagon) defect, as evidenced by the strong electron−hole conductance asymmetry. Such an effect, already observed in nanotube junctions,[32] is clearly due to the charge transfer taking place in the $\pi - \pi^*$ bands when odd-membered rings are embedded in a perfect hexagonal network. According to the Mulliken decomposition of the electronic density, a slight excess of π-electrons (+0.152) is found on the pentagonal ring and a small deficit of π-electrons (−0.135) is reported on the heptagon. Five-membered rings (D_1) are thus attractive (acceptor character), seven-membered rings (D_2) are repulsive of electrons (donor character),[33] and even-membered rings (D_3, D_4) are predicted to be neutral in a planar hexagonal network.

For all cases, the total and local densities-of-states have been computed (shown for D_1 and D_2 in Figure 1a,b) and reveal the energy position of quasibound states which are responsible for the conductance drops.[34] The charge density contour plot (Figure 1c) shows the electronic state incident from the left and totally reflected by the quasibound state at the energy indicated by an arrow in Figure 1b. The backscattering associated with quasibound states is a general mechanism, and we forecast the acceptor, donor, and neutral characteristics reported respectively for the D_1, D_2, and $D_{3/4}$ topologies to be robust with respect to the ribbon width. However, the broadening of the conductance dips is expected to decrease for larger ribbon widths. The intensity of the observed electron−hole conductance asymmetry is thus likely to depend on the actual ribbon geometry.

The high chemical reactivity of defects such as D_1 and D_2 is further explored by assuming a dihydrogenation of the carbon atom sitting at the edge. Resulting conductance profiles for the new defects D_{1H} (Figure 1f) and D_{2H} (Figure 1g) strongly differ from the monohydrogenated cases (D_1 and D_2). Indeed, in the presence of additional passivation the conductance is fully restored for D_{1H}, whereas the signature for D_{2H} becomes similar to that of D_3. In both cases, the initial strong reduction of electron or hole conductance is markedly sup-

pressed. This clearly suggests a possibility to tune the transport properties from a metallic to a truly insulating state (or vice versa) upon varying the coverage of monotamic hydrogen, as recently discussed experimentally for 2D graphene.[29]

The Clar's sextet representation[35,36] (Figure 1 (insets)) provides a pictorial scheme to understand the impact of edge defects[37] on the transport properties. The Clar's theory proposes a simplified description of the π-electronic structure of hydrocarbons on the basis of the resonance patterns that maximize the number of benzenoid sextets drawn for the system. The benzenoid sextets, shown as plain circles in the insets of Figure 1, are defined as the carbon hexagons that stem from the resonance between two Kekulé structures with alternating single and double bonds. These are associated with a benzene-like delocalization of the π electrons over the carbon ring. As a consequence, the Clar's representation provides direct insights into the aromaticity of the π-electronic structure. According to the Clar's theory, pristine aGNRs are fully benzenoid (*i.e.*, all π-orbitals are involved in a benzenoid sextet). This ideal picture is not preserved in the presence of defects. Upon the introduction of the D_1 and D_2 topologies, the bonding of the aGNR can be seen as the superposition of two mirroring Kekulé structures that partially destroy the benzenoid character of the aGNRs (Figure 1a,b). By increasing the localization of π electrons in carbon−carbon double bonds, such defects destroy the local aromaticity at the ribbon edge and are thus expected to have a large effect on the $\pi-\pi^*$ conduction channels. On the contrary, the dihydrogenation of defects D_1 and D_2 restores the complete benzenoid character of the ribbon as illustrated by Clar's sextet representations (Figure 1f,g).

To further substantiate the effect of these topological defects on the mesoscopic transport properties, one needs to explore the behavior of long disordered aGNRs with random distribution of edge defects. In Figure 1, the conductance of 500 nm long disordered aGNRs containing 30 defects (blue lines) are superimposed to the single defect results (red lines). Computed conductances are averaged over 20 different disorder configurations. The original conductance fingerprints of the considered defects are further exacerbated when longitudinal disorder is introduced, resulting for D_1 (D_2) in an almost fully suppressed hole (electron) conduction for low defect density.

Ab initio transport calculations are highly computationally demanding, and the elaboration of an accurate tight-binding (TB) model is therefore extremely useful for achieving a complete mesoscopic study. Though most of previous studies rely on a simple topological nearest-neighbor TB Hamiltonian to derive the conductance patterns of mesoscopic GNRs, when compared to *ab initio* results, this turns out to yield a wrong description of transport properties in the case of non-

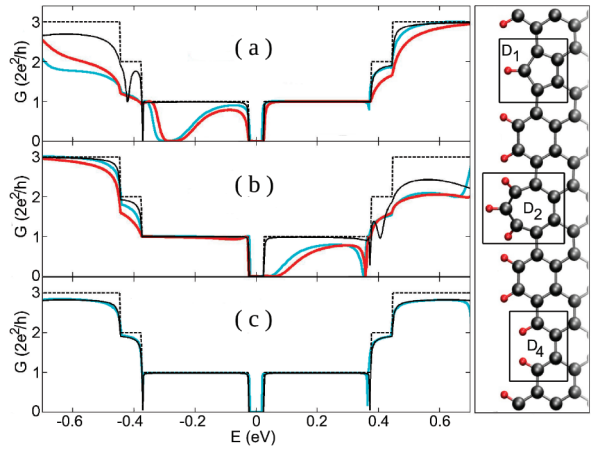

Figure 2. Conductance profiles of 35-aGNR for three different isolated defects: (top panel) D_1, (middle panel) D_2, (bottom panel) D_4. Ball-and-stick models of the defects are illustrated in the right panel. Black dashed lines represent the conductance of the pristine ribbon. The *ab initio* computed curves are reported in turquoise. Black and red lines correspond to the topological and fitted TB models, respectively.

neutral defects. Figure 2 shows the conductance profiles of three different defects (D_1, D_2, and D_4) computed either within a topological TB model (black solid lines) or within an adjusted TB model (red solid lines). Though the agreement between *ab initio* and topological TB results is good for the D_4 defect, strong discrepancies are found for D_1 and D_2 defects. In the latter cases, the topological model leads to a severe underestimation of the backscattering efficiency. In contrast, the fitting of the TB parameters allows the reproduction of the conductance evaluated by means of the full density functional theory (DFT) Hamiltonian.[38]

Within the fitted TB model, the transport properties of disordered aGNRs are investigated by considering lengths varying up to $L = 5$ μm and random distribution of defects with a density of 6×10^{-2} nm^{-1}. Figure 3 and Figure 4 display the conductance of long disordered aGNRs (averaged over 100 different configurations), as a function of energy and ribbon length. Besides, the regions of the (L, E)-plane where the conductance is experimentally insignificant (*i.e.*, $G(E) \leq 0.01G_0$) are delineated by white lines. This allows us to determine the length dependent conduction gaps.

In the presence of charged defects (*i.e.*, pentagon (D_1) and heptagon (D_2) defects), the conductance scaling behavior of long disordered aGNRs presents a striking electron−hole asymmetry. Figure 3 clearly shows that depending on the energy at which carriers are injected, the electronic transport ranges from ballistic to localized regimes. In D_1-defected aGNRs (Figure 3a), the propagation of electrons in the first plateau remains quasi-ballistic up to a length $L > 5$ μm. As a consequence of the acceptor character of D_1 defects, the hole conduction, in the same energy window, is almost fully suppressed for length $L < 0.5$ μm. In contrast, in the presence of D_2 defects (Figure 3b), holes in the first

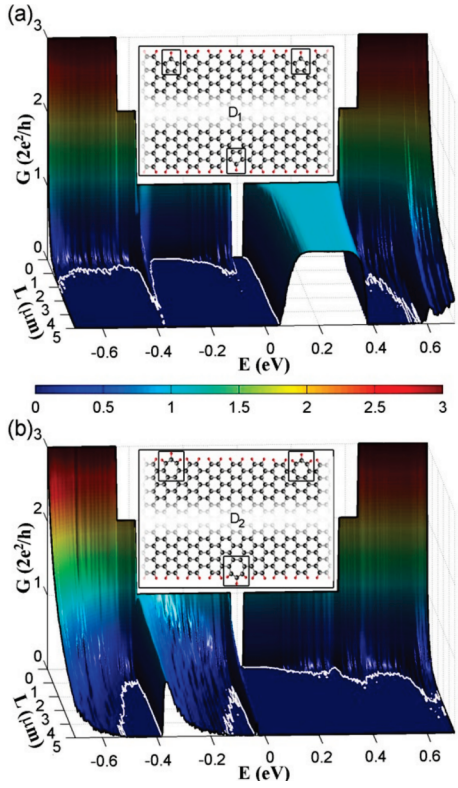

Figure 3. Conductance of a 35-aGNR with a 6 × 10^{-2} nm^{-1} density of (a) D_1 defects and (b) D_2 defects. The conductance is given as a function of the carrier energy (*E*) and the length of the ribbon (*L*). *G*(*L*, *E*) has been averaged over 100 different defect distributions. The white lines delineate the (*L*, *E*) regions for which the conductance value $G \leq 0.01G_0$ (criterion for the experimental conduction gap[9]).

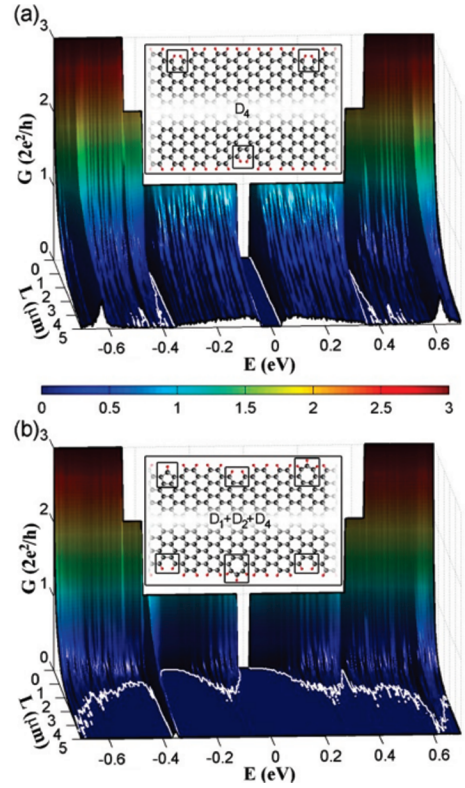

Figure 4. Conductance of a 34-aGNR with a 6 × 10^{-2} nm^{-1} density of (a) D_4 defects and (b) mix of {D_1, D_2, D_4} defects. The conductance is given as a function of the carrier energy (*E*) and the length of the ribbon (*L*). *G*(*L*, *E*) has been averaged over 100 different defect distributions. The white lines delineate the (*L*, *E*) regions for which the conductance value $G \leq 0.01G_0$ (criterion for the experimental conduction gap[9]).

plateau remain conductive up to length $L > 5$ μm, while the donor character of the D_2 defects involves the suppression of electron conduction in the same energy window. Obviously, such disordered edge defect profiles with a single defect type are rather unlikely, but this example shows however that spectacular fluctuations of transport length scales occur in some specific situations.

The comparison with more realistic defect distributions is rather instructive. Figure 4 details the conductance scaling in the presence of a random distribution of D_4 defects (Figure 4a), and a mix of three types of defects {D_1, D_2, and D_4} (Figure 4b) for the same edge defect density. For both defect distributions, the conductance decay is rather homogeneous within the first electron and hole plateaus. However, while the marked electron−hole asymmetries associated with the D_1 and D_2 defects compensate each other, the presence of odd-membered rings continues to crucially impact the electron and hole localization. This appears evident by looking at the white line in the (*L*, *E*)-plane. The presence of defects that are noncompliant with the benzenoid character of aGNRs (*i.e.*, D_1 and D_2) thus appears to strongly impinge the ballistic propagation of carriers, even for the low defect concentration considered here. This is further emphasized by the estimated localization lengths that are reported in Figure 5 as a function of the carrier energy. While the distribution of D_4 defects gives rise to a localization length $\xi \approx 1$ μm for low energy carriers, the introduction of charged defects strongly reduces the average value in the [−0.5,0.5] eV energy window. Note that the fluctuations of ξ in corre-

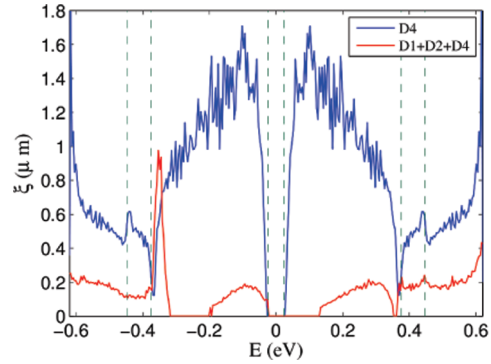

Figure 5. Localization length ξ for a 35-aGNR with a 6 × 10^{-2} nm^{-1} density of D_4 defects (blue line) and a mix of {D_1, D_2, D_4} defects. The vertical dashed lines correspond to the position of the van Hove singularities. In some energy regions, ξ is very short (below 100 nm), and it cannot be extracted from the data. In this case, we set ξ = 0. As already arguable from Figure 4, the localization length for the D_4 defects is up to almost 1 order of magnitude longer than in the case of mixed defects.

spondence of the van Hove singularities for D_4 defects are due to the increased scattering induced by the high density-of-states at these points. In the case of the mixed disorder, these fluctuations are absent or considerably reduced owing to the strong smearing effect that disorder produces in the density-of-states.

CONCLUSIONS

The electronic and quantum transport properties of edge disordered graphene nanoribbons have been investigated using both fully *ab initio* techniques and accurately parametrized tight-binding models. Single topological defects such as pentagons and heptagons are predicted to induce a strong electron−hole transport asymmetry. Besides, conduction gaps driven by defect-induced localization effects have been shown to depend not only on the defect density and ribbon length but also on the geometry and chemical reactivity of edge imperfections. The above analysis is drawn from physical processes that are general in essence. The scope of the results should therefore extend beyond the edge profiles considered in this study. In particular, we forecast similar fluctuations of the conductance to be reported for other GNR topologies whose ground-state π-electronic structure is aromatic according to Clar's rule. Note that the GNR topologies that come with partially filled states at the edge are known to break the graphene aromaticity.[22] Therefore, our conclusions and their rationalization in terms of the Clar's sextet theory are likely to not apply for such ribbon geometries. In addition, hydrogenation has been identified as a new route to tune the robustness of the electronic conductance against edge roughness. As recently reported experimentally in 2D graphene,[29] the controlled deposition of monotamic hydrogen is a key ingredient to explore a metal/insulator transition in these materials. Similar study on graphene ribbons would bring a better understanding of low dimensional transport.

METHODS

Electronic structures of the edge-reconstructed ribbons are computed by using the DFT within the generalized-gradient approximation as implemented in the SIESTA code.[39] A basis set of double-ζ quality and norm-conserving pseudopotentials are used. The integration of the first Brillouin zone is achieved through a summation over a regular grid of 24 *k*-points. The ribbon geometries are relaxed such that the residual forces on atoms become lesser than 0.01 eV/Å; 12 Å of vacuum between GNRs in neighboring cells is taken.

At zero temperature and in the low bias limit, the conductance is given by $G(E) = G_0T(E)$, where $T(E)$ denotes the transmission coefficient at a given energy E ($G_0 = 2e^2/h$ is the conductance quantum). The conductance fingerprints of single defects are computed within the Green's function formalism adopted by the SMEAGOL code.[40] For that purpose, the defective supercells are connected to semi-infinite GNR-based leads. The total density-of-states stem from the trace of the retarded Green's functions ($\rho(E) = \mathrm{Tr}[G_{rr'}(E)]$). Within the Green's function formalism, the transmission eigenchannels can be readily derived from the spectral functions associated with the scattering region.[41]

The electronic structures and conductance patterns discussed in the paper assume a 2-fold spin-degeneracy of the electronic states. Spin-polarized DFT calculations have been performed in order to assess the robustness of the results. Upon the explicit consideration of the spin degree of freedom, all the edge profiles considered here do preserve the spin-degeneracy with the exception of the D_2 defect that involves a spin-polarized electronic density. Though the spin density distribution induces a splitting of the defect-induced quasibound states, the global shape of the transmission function is likely to remain globally the same. Therefore, our conclusions regarding the conduction properties of aGNRs should not be affected by the spin-degeneracy approximation.

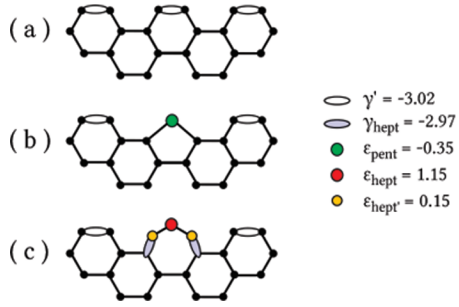

Figure 6. Schematic representation of three edge topologies and the associated adjusted tight-binding parameters: (a) pristine armchair edge, (b) D_1 defect, and (c) D_2 defect. Black dots and lines represent unadjusted onsite energies ($\varepsilon = 0$ eV) and hopping integrals ($\gamma = -2.7$ eV), respectively. All values are given in eV.

The computation of the mesoscopic conductance is performed within the Landauer−Büttiker formalism and has been implemented at both first principles and tight-binding (TB) levels.[31,42,43] In the former case, *ab initio* self-consistent Hamiltonians corresponding to defective supercells are used to build long (~500 nm) aGNRs containing 30 randomly distributed defects. In the latter case, a suited nearest-neighbor TB Hamiltonian has been derived. Owing to its use of atomic basis orbitals for the expansion of the electronic density, the SIESTA code provides a self-consistent *ab initio* Hamiltonian of tight-binding type.[39] Therefore, the renormalized onsite and hopping energies can be readily extracted from the p_z components of the *ab initio* Hamiltonian associated with the Γ-point. The fitted TB parameters are detailed in Figure 6. On the one hand, the fine-tuning of the on-site energies allows dealing with the defect-induced charge transfer. On the other hand, the variation of the hopping parameters accounts for the local modifications of the interatomic distance. By reducing the computational costs, the TB technique enables the investigation of disordered ribbons with lengths up to several micrometers.

Acknowledgment. J.-C.C. and S.R. acknowledge funding from the Belgium F.R.S.-FNRS and the Alexander Von Humboldt Foundation, respectively. A.C. thanks the CARNOT Institute (LETI), and A.L.B the Marie-Curie fellowship CHEMTRONICS programme. B.B. acknowledges financial support from the Juan de la Cierva Program and the FIS2008-05805 Contract of the Spanish MICINN. Part of this work was conducted within the "Quantum Effects in Clusters and Nanowires" Belgian Program on Interuniversity Attraction Poles (PAI6) and the ARC sponsored by the Communauté Française de Belgique. Part of this work has been carried out within the NANOSIM_GRAPHENE project ANR-09-NANO-016-01 funded by the French National Agency (ANR) in the frame of its 2009 programme in Nanosciences,Nanotechnologies & Nanosystems (P3N2009) The CSIM (Université Catholique de Louvain) and CEA/CCRT high performance computational resources are acknowledged.

REFERENCES AND NOTES

1. Iijima, S. Helical microtubules of graphitic carbon. *Nature* **1991**, *354*, 56–58.
2. Charlier, J.-C.; Blase, X.; Roche, S. Electronic and transport properties of nanotubes. *Rev. Mod. Phys.* **2007**, *79*, 677.
3. Geim, A. K. Graphene: Status and prospects. *Science* **2009**, *324*, 1530–1534.
4. Castro Neto, A. H.; Guinea, F.; Peres, N. M. R.; Novoselov, K. S.; Geim, A. K. The electronic properties of graphene. *Rev. Mod. Phys.* **2009**, *81*, 109–162.
5. Nakada, K.; Fujita, M.; Dresselhaus, G.; Dresselhaus, M. S. Edge state in graphene ribbons: Nanometer size effect and edge shape dependence. *Phys. Rev. B* **1996**, *54*, 17954–17961.
6. Wakabayashi, K. Electronic transport properties of nanographite ribbon junctions. *Phys. Rev. B* **2001**, *64*, 125428.
7. Sasaki, K.; Murakami, S.; Saito, R. Stabilization mechanism of edge states in graphene. *Appl. Phys. Lett.* **2006**, *88*, 113110.
8. Munoz-Rojas, F.; Jacob, D.; Fernandez-Rossier, J.; Palacios, J. J. Coherent transport in graphene nanoconstrictions. *Phys. Rev. B* **2006**, *74*, 195417.
9. Han, M. Y.; Ozyilmaz, B.; Zhang, Y. B.; Kim, P. Energy band-gap engineering of graphene nanoribbons. *Phys. Rev. Lett.* **2007**, *98*, 206805.
10. Lemme, M. C.; Echtermeyer, T. J.; Baus, M.; Kurz, H. A graphene field-effect device. *IEEE Electron Dev. Lett.* **2007**, *28*, 282–284.
11. Wang, X. R.; Ouyang, Y. J.; Li, X. L.; Wang, H. L.; Guo, J.; Dai, H. J. Room-temperature all-semiconducting sub-10-nm graphene nanoribbon field-effect transistors. *Phys. Rev. Lett.* **2008**, *100*, 206803.
12. Wimmer, M.; Adagideli, I.; Berber, S.; Tomanek, D.; Richter, K. Spin currents in rough graphene nanoribbons: Universal fluctuations and spin injection. *Phys. Rev. Lett.* **2008**, *100*, 177207.
13. Yazyev, O. V.; Katsnelson, M. I. Magnetic correlations at graphene edges: Basis for novelspintronics devices. *Phys. Rev. Lett.* **2008**, *100*, 047209.
14. Son, Y. W.; Cohen, M. L.; Louie, S. G. Energy gaps in graphene nanoribbons. *Phys. Rev. Lett.* **2006**, *97*, 216803.
15. Barone, V.; Hod, O.; Scuseria, G. E. Electronic structure and stability of semiconducting graphene nanoribbons. *Nano Lett.* **2006**, *6*, 2748–2754.
16. White, C. T.; Li, J. W.; Gunlycke, D.; Mintmire, J. W. Hidden one-electron interactions in carbon nanotubes revealed in graphene nanostrips. *Nano Lett.* **2007**, *7*, 825–830.
17. Dubois, S. M. M.; Zanolli, Z.; Declerck, X.; Charlier, J. C. Electronic properties and quantum transport in graphene-based nanostructures. *Eur. Phys. J. B* **2009**, *72*, 1–24.
18. Areshkin, D. A.; Gunlycke, D.; White, C. T. Electronic properties and quantum transport in graphene-based nanostructures. *Nano Lett.* **2007**, *7*, 204–210.
19. Evaldsson, M.; Zozoulenko, I. V.; Xu, H. Y.; Heinzel, T. Electronic properties and quantum transport in gGraphene-based nanostructures. *Phys. Rev. B* **2008**, *78*, 161407.
20. Mucciolo, E. R.; Neto, A. H. C.; Lewenkopf, C. H. Electronic properties and quantum transport in graphene-based nanostructures. *Phys. Rev. B* **2009**, *79*, 075407.
21. Cresti, A.; Roche, S. Electronic properties and quantum transport in graphene-based nanostructures. *Phys. Rev. B* **2009**, *79*, 233404.
22. Wassmann, T.; Seitsonen, A. P.; Saitta, A. M.; Lazzeri, M.; Mauri, F. Electronic properties and quantum transport in graphene-based nanostructures. *Phys. Rev. Lett.* **2008**, *101*, 096402.
23. Koskinen, P.; Malola, S.; Hakkinen, H. Self-passivating edge reconstructions of graphene. *Phys. Rev. Lett.* **2008**, *101*, 115502.
24. Huang, B.; Liu, M.; Su, N. H.; Wu, J.; Duan, W. H.; Gu, B. L.; Liu, F. Quantum manifestations of graphene edge stress and edge instability: A first-principles study. *Phys. Rev. Lett.* **2009**, *102*, 166404.
25. Koskinen, P.; Malola, S.; Hakkinen, H. Evidence for graphene edges beyond zigzag and arm chair. *Phys. Rev. B* **2009**, *80*, 073401.
26. Kobayashi, Y.; Fukui, K.; Enoki, T.; Kusakabe, K. Edge state on hydrogen-terminated graphite edges investigated by scanning tunneling microscopy. *Phys. Rev. B* **2006**, *73*, 125415.
27. Casiraghi, C.; Hartschuh, A.; Qian, H.; Piscanec, S.; Georgi, C.; Fasoli, A.; Novoselov, K. S.; Basko, D. M.; Ferrari, A. C. Raman spectroscopy of graphene edges. *Nano Lett.* **2009**, *9*, 1433–1441.
28. Liu, Z.; Suenaga, K.; Harris, P. J. F.; Iijima, S. Open and closed edges of graphene layers. *Phys. Rev. Lett.* **2009**, *102*, 015501.
29. Bostwick, A.; McChesney, J. L.; Emtsev, K. V.; Seyller, T.; Horn, K.; Kevan, S. D.; Rotenberg, E.; Rotenberg, E. Quasiparticle transformation during a metal-insulator transition in graphene. *Phys. Rev. Lett.* **2009**, *103*, 056404.
30. Elias, D. C.; Nair, R. R.; Mohiuddin, T. M. G.; Morozov, S. V.; Blake, P.; Halsall, M. P.; Ferrari, A. C.; Boukhvalov, D. W.; Katsnelson, M. I.; Geim, A. K.; Novoselov, K. S. Control of graphene's properties by reversible hydrogenation: evidence for graphane. *Science* **2009**, *323*, 610–613.
31. Lopez-Bezanilla, A.; Triozon, F.; Latil, S.; Blase, X.; Roche, S. Effect of the chemical functionalization on charge transport in carbon nanotubes at the mesoscopic scale. *Nano Lett.* **2009**, *9*, 940–944.
32. Charlier, J. C.; Ebbesen, T. W.; Lambin, P. Structural and electronic properties of pentagon−heptagon pair defects in carbon nanotubes. *Phys. Rev. B* **1996**, *53*, 11108–11113.
33. Tamura, R.; Tsukada, M. Disclinations of monolayer graphite and their electronic states. *Phys. Rev. B* **1994**, *49*, 7697–7708.
34. Choi, H. J.; Ihm, J.; Louie, S. G.; Cohen, M. L. Defects, quasibound states, and quantum conductance in metallic carbon nanotubes. *Phys. Rev. Lett.* **2000**, *84*, 2917–2920.
35. Clar, E. *Polycyclic Hydrocarbons*; Academic Press: London, 1964.
36. Clar, E. *The Aromatic Sextet*; Wiley: New York, 1972.
37. Baldoni, M.; Sgamellotti, A.; Mercuri, F. Electronic properties and stability of graphene nanoribbons: An interpretation based on Clar sextet theory. *Chem. Phys. Lett.* **2008**, *464*, 202–207.
38. Avriller, R.; Roche, S.; Triozon, F.; Blase, X.; Latil, S. Low-dimensional quantum transport properties of chemically-disordered carbon nanotubes: From weak to strong localization regimes. *Mod. Phys. Lett. B* **2007**, *21*, 1955–1982.
39. Ordejon, P.; Artacho, E.; Soler, J. M. Self-consistent order-*N* density-functional calculations for very large systems. *Phys. Rev. B* **1996**, *53*, 10441–10444.
40. Rocha, A. R.; Garcia-Suarez, V. M.; Bailey, S.; Lambert, C.; Ferrer, J.; Sanvito, S. Spin and molecular electronics in atomically generated orbital landscapes. *Phys. Rev. B* **2006**, *73*, 085414.
41. Paulsson, M.; Brandbyge, M. Transmission eigenchannels from nonequilibrium Green's functions. *Phys. Rev. B* **2007**, *76*, 115117.
42. Markussen, T.; Rurali, R.; Brandbyge, M.; Jauho, A. P. Electronic transport through Si nanowires: Role of bulk and surface disorder. *Phys. Rev. B* **2006**, *74*, 245313.
43. Biel, B.; Triozon, F.; Blase, X.; Roche, S. Chemically induced mobility gaps in graphene nanoribbons: A route for upscaling device performances. *Nano Lett.* **2009**, *9*, 2725–2729.